PAPER

Check for updates

Scalable, epitaxy-preserving transfer of freestanding perovskite and layered oxide membranes with tunable strain

Habib Rostaghi Chalaki,[a] Ebenezer Seesi,[a] Avari Suber,[a] Sang-Hoon Nam,[b] Yo-Han Suh[c] and Dongkyu Lee ID *[a]

Freestanding single-crystal transition metal oxide membranes enable mechanically flexible devices and heterogeneous integration on diverse substrates, yet scalable transfer without cracking or wrinkling while preserving epitaxy and transport remains challenging. Here, we demonstrate a modified wet release-and-transfer process that transfers large-area epitaxial oxide films (up to 25 mm^2) onto silicon, insulating, and flexible substrates using compositionally engineered, water-soluble sacrificial layers and a single polypropylene carbonate (PPC) support layer. The one-layer PPC scaffold enables robust handling and solvent-based removal without a heating step, simplifying processing and limiting thermal exposure. By selecting sacrificial layer chemistry and controlling whether the sacrificial layer remains strained or relaxes, we tune residual strain from compressive to tensile across multiple perovskite and layered oxide membranes, including $La_{0.8}Sr_{0.2}CoO_3$, $La_{0.7}Ca_{0.2}Ni_{0.25}Ti_{0.75}O_3$, $SrTiO_3$, $Sr_{0.95}Ti_{0.76}Ni_{0.05}Nb_{0.19}O_3$, and $La_{1.85}Sr_{0.15}CuO_4$, as verified by high-resolution X-ray diffraction and reciprocal space mapping. Systematic analysis of defects formed during release and transfer shows that crack and wrinkle formation is strongly strain-dependent and is further influenced by membrane mechanical compliance and transfer constraints. Finally, temperature-dependent in-plane conductivity measurements demonstrate that defect-minimized membranes retain film-like transport, crack-dominated membranes exhibit pronounced degradation, and wrinkle-dominated membranes show only modest, system-dependent changes. This study establishes a strain-programmable, single-crystal oxide membrane platform that is broadly applicable across multiple perovskite and layered oxide systems and transferable to silicon, insulating substrates, and flexible supports, enabling heterogeneous integration and mechanically compliant oxide electronics.

Introduction

Advances in epitaxial growth of single-crystalline thin film heterostructures have enabled many technological breakthroughs in modern solid-state electronic and photonic devices over the past few decades.[1–3] In particular, epitaxial transition metal oxide (TMO) thin films provide a versatile platform for coupling order parameters across interfaces, giving rise to emergent and tunable functionalities such as metal–insulator transitions,[4–6] mixed ionic and electronic conductivity,[7–10] superconductivity,[11–13] and multiferroicity.[14–16] These opportunities are driving increasing interest in integrating multifunctional epitaxial TMO heterostructures into next-generation device architectures.

Despite this promise, the conventional film-on-substrate scheme offers a limited set of control parameters, mainly due to the availability and compatibility of single-crystalline substrates.[17–19] This constraint restricts accessible strain states, symmetry matching, and integration onto non-epitaxial device platforms, ultimately limiting the range of functional responses attainable through epitaxial design. Substrate-isolated, free-standing oxide membranes offer an alternative route. By decoupling epitaxial films from rigid substrates, they enable transfer onto diverse substrates and multilayer stacking, introduce mechanical flexibility, and open pathways to functionalities that are difficult or impossible to achieve in clamped films.[20–22]

Among the various fabrication approaches, wet etching of water-soluble sacrificial crystalline layers has emerged as a particularly reliable strategy to produce large-area, single-crystalline TMO membranes with minimal contamination and defects.[23,24] In this method, epitaxial films are synthesized on a sacrificial layer, released by selectively dissolving the sacrificial layer, and transferred onto a target substrate.[25] However, structural distortions

[a] Department of Mechanical Engineering, University of South Carolina, Columbia, SC 29208, USA. E-mail: dongkyu@cec.sc.edu

[b] Research Laboratory of Electronics, Massachusetts Institute of Technology, Cambridge, MA 02139, USA

[c] Smart Electronics Research Center, Korea Electronics Technology Institute (KETI), Jeonju 54853, Republic of Korea

and defect formation can arise during each step, often preventing the creation of freestanding membranes free of cracks and wrinkles.[26,27]

First, during film growth, epitaxy can be optimized by controlling deposition parameters such as temperature and background pressure.[28,29] Beyond synthesis, mechanical factors become increasingly important during release and transfer. Membrane integrity is influenced by elastic stiffness (often approximated by Young's modulus) together with thickness, residual strain, and interfacial adhesion.[30,31] Rather than assigning membrane quality to stiffness alone, it is more appropriate to view stiffness as one design parameter that can alter the balance between competing failure modes (e.g., fracture *versus* buckling) in conjunction with strain state and processing conditions. Importantly, many studies have focused on prototypical $SrTiO_3$ (STO) or closely related systems, leaving limited comparative understanding of how mechanical stiffness and oxide chemistry collectively impact membrane quality across broader classes of TMOs.[26,32–36]

Second, the epitaxial strain between the film and the sacrificial layer critically affects defect formation during release.[37,38] As the sacrificial layer is selectively etched, the film transitions from a clamped state to a freestanding state, generating strain relaxation and, in many cases, substantial strain gradients, especially near boundaries between released and unreleased regions. These gradients can drive either out-of-plane buckling (wrinkling) or in-plane fracture (cracking), depending on the magnitude and sign of residual strain, thickness, and mechanical constraint from the support layer.[26,39] $Sr_3Al_2O_6$ (SAO), which has a pseudo-perovskite structure (Pa-3) with a cubic unit cell (a = 15.844 Å, corresponding to $a/4$ = 3.961 Å), is a commonly used water-soluble sacrificial layer.[25] SAO offers compatibility with perovskite oxides and can be chemically tuned by A-site substitution (*e.g.*, Ca or Ba) to modulate lattice parameters and, consequently, epitaxial mismatch.[26,40–42] However, a systematic understanding of how compositional tuning controls strain relaxation pathways and membrane defect formation remains limited.

Third, polymer support layers, which are essential for handling, pick-up, and stamping, strongly influence membrane quality during both release and transfer. In typical fabrication processes, a polymer layer is applied to the film surface to provide mechanical support during sacrificial layer dissolution and to enable transfer onto a target substrate.[35,43,44] Yet the polymer can also introduce additional stresses and constraints that promote wrinkling or cracking, and the transfer step often becomes the most yield-limiting stage due to the coupled roles of polymer viscoelasticity, peeling kinetics, adhesion, and polymer removal.[45] In particular, support strategies based on polydimethylsiloxane (PDMS) coated with thermoplastic layers (*e.g.*, polypropylene carbonate (PPC) or polycaprolactone) are widely used, but process complexity, especially heating-assisted removal and sensitivity to peeling conditions, can limit scalability and reproducibility.[20,25,46,47]

Achieving large-area, defect-minimized freestanding oxide membranes therefore requires simultaneous control over film synthesis, sacrificial layer design and strain relaxation during release, and polymer support mechanics during transfer. In this study, we address these coupled challenges by developing a scalable transfer strategy that combines a single PPC support layer with compositionally engineered $Sr_{3-x}Ca_xAl_2O_6$ (SCAO, x = 0–3) sacrificial layers, enabling systematic modulation of epitaxial strain and relaxation behavior. We demonstrate freestanding membranes from multiple epitaxial ABO_3 perovskite and A_2BO_4 Ruddlesden–Popper oxides and evaluate defect formation in terms of cracking and wrinkling under controlled processing conditions. We further evaluate in-plane electrical conductivity of freestanding membranes in multiple oxide systems, directly assessing transport retention after transfer. Together, this work advances both the scalable processing strategy and the mechanistic understanding needed to produce strain-programmable, large-area epitaxial oxide membranes for heterogeneous integration and flexible oxide electronics.

Experimental

Growth of epitaxial ABO_3 and A_2BO_4 thin films on water-soluble sacrificial layers

To systematically control epitaxial strain in the functional oxides, a series of water-soluble SCAO sacrificial layers were synthesized on either (001) STO or $LaAlO_3$ (LAO) substrates by pulsed laser deposition (PLD), depending on the lattice parameter of the target films. Strain in the sacrificial layers was controlled by varying their thickness. SCAO sacrificial layers were deposited at 30 or 120 nm, selected case-by-case to achieve the desired sacrificial layer strain state for each oxide system. Thinner layers were used to promote substrate-clamped (more coherently strained) SCAO, whereas thicker layers were used to promote partial-to-near-complete relaxation toward the composition-dependent lattice parameter (Fig. S1). The resulting sacrificial layer and film strain states were assessed by reciprocal space mapping for each heterostructure, and the corresponding lattice parameters and lattice mismatches are summarized in Table S1. All SCAO layers were deposited at 750 °C using a KrF excimer laser (λ = 248 nm) with a repetition rate of 5 Hz and a laser fluence of $\sim$1 J cm^{-2}. The oxygen partial pressure (pO_2) was 10^{-6} Torr for $Sr_3Al_2O_6$ (SAO) and $Sr_2CaAl_2O_6$ (S2C1AO), and 100 mTorr for $SrCa_2Al_2O_6$ (S1C2AO) and $Ca_3Al_2O_6$ (CAO).

Epitaxial thin films ($\sim$50 nm) with four ABO_3 oxides, $Sr_{0.95}Ti_{0.76}Ni_{0.05}Nb_{0.19}O_3$ (STNNO), $La_{0.7}Ca_{0.2}Ni_{0.25}Ti_{0.75}O_3$ (LCNTO), STO, and $La_{0.8}Sr_{0.2}CoO_3$ (LSCO), and one A_2BO_4 oxide, $La_{1.85}Sr_{0.15}CuO_4$ (LSCuO), were deposited on the water-soluble sacrificial layers. To impose controlled compressive-to-tensile strain, each film was grown on a selected SCAO sacrificial layer based on its lattice mismatch. All film/sacrificial layer/substrate combinations are listed in Table S2. Epitaxial films were deposited at 700 °C, 10 Hz, and $\sim$1 J cm^{-2} fluence under pO_2 = 100 mTorr. After deposition, the samples were cooled to room temperature in the PLD chamber for 1 h under pO_2 = 100 mTorr.

Structural and surface morphological analysis of the films before and after the transfer

Phase purity and crystallography of the films were examined using high-resolution X-ray diffraction (HRXRD) with a four-circle

diffractometer in both in-plane and out-of-plane configurations. Details of lattice parameter and strain extraction are provided in the SI. Film thickness was characterized by X-ray reflectivity (XRR) measurements. To assess the strain state of the films, XRD reciprocal space maps (RSM) were performed around the substrates' 103 Bragg reflections. Surface morphology and membrane integrity before and after transfer were examined by optical microscopy and scanning electron microscopy (SEM, Zeiss Gemini FE500).

Fabrication and transfer of freestanding ABO$_3$ and A$_2$BO$_4$ membranes

To support membrane release and transfer while minimizing process complexity, a single PPC layer was used as the mechanical support. PPC solutions with concentrations of 15 wt% and 30 wt% were evaluated at spin speeds from 1000–5000 rpm (30 s for all conditions). PPC support conditions were optimized using STO as a model system, and the resulting standard condition (15 wt% PPC, 4000 rpm, 30 s) was used for all oxide systems. After spin coating, samples were air-dried for 16 h and then immersed in deionized (DI) water to dissolve the sacrificial layer. Release time depended on sacrificial layer composition and thickness, ranging from ~24 h for 30-nm-thick SAO to ~240 h for 120-nm-thick CAO.

After complete release, floating PPC-supported membranes were transferred onto silicon and sapphire substrates and allowed to adhere at room temperature. The PPC support was removed using chloroform, followed by sequential rinsing with isopropanol and ethanol. In addition, a direct transfer route to flexible substrates was explored by laminating polyimide (PI) tape onto the as-grown film surface prior to water immersion, enabling membrane pick-up without post-transfer polymer removal.

Electrical conductivity measurements of epitaxial films and freestanding membranes

Electrical conductivity (σ) of freestanding membranes transferred onto sapphire was compared with that of epitaxial reference films. To establish comparable relaxed epitaxial baselines, epitaxial STNNO, LSCO, LSCuO, STO, and LCNTO films were deposited on (001) (LaAlO$_3$)$_{0.3}$(SrAl$_{0.5}$Ta$_{0.5}$O$_3$)$_{0.7}$ (LSAT) substrates. To minimize strain-related contributions to the conductivity measurements, the epitaxial reference films were deposited to a thickness of ~300 nm, which is sufficient to achieve strain relaxation. σ was measured in air from 450 to 700 °C using a van der Pauw electrode configuration with a DC voltage/current source/monitor (Keithley 2450 Sourcemeter).

Results and discussion

Epitaxial synthesis of strain-controlled thin films

To enable strain-controllable freestanding membranes, we first established growth windows for the water-soluble SCAO sacrificial layers, which act as epitaxial templates that set the residual strain state of the oxide films. The pseudo-cubic lattice

parameter of SCAO ($a_{pc} = a/4$) is tunable from 3.819 to 3.961 Å through A-site substitution, where Ca substitution reduces the lattice size relative to Sr (Fig. 1a).[48] This tunability provides a practical handle to systematically vary lattice mismatch and thus residual epitaxial strain in the overgrown oxides. Since unintended secondary phases in the sacrificial layer would complicate both lattice-parameter control and dissolution behavior during release, we verified the phase purity of SCAO by out-of-plane θ–2θ scans (Fig. S2). SAO and S2C1AO grown under low pO_2 showed only reflections consistent with the targeted A$_3$Al$_2$O$_6$ phase. In contrast, Ca-rich layers (S1C2AO and CAO) occasionally exhibited an additional reflection consistent with an A$_4$Al$_2$O$_7$-type secondary phase. This secondary peak was eliminated by post-annealing at 750 °C under pO_2 = 100 mTorr.

After optimizing the growth conditions for the sacrificial layers, thin films of LSCO, LCNTO, STO, LSCuO, and STNNO were deposited on selected SCAO layers. Out-of-plane XRD θ–2θ scans confirmed high-quality epitaxial growth for all films, showing only (00l) peaks indicative of (00l)-oriented films on (001) substrates (Fig. 1b). The in-plane epitaxial relationship is further supported by ϕ scans collected from both the films and their corresponding SCAO sacrificial layers, which exhibited clear four-fold symmetry and indicated well-defined in-plane crystallographic alignment among film, sacrificial layer, and substrate (Fig. 1c and d). Residual strain and relaxation were assessed using XRD reciprocal space maps (RSM) around the substrates' 103 Bragg reflections (Fig. 1e–i).

The combined θ–2θ and RSM analyses indicate that the residual strain state of each film depends on the in-plane lattice parameter of the underlying SCAO sacrificial layer, which depends on whether the sacrificial layer remains coherently strained to the substrate or relaxes toward its bulk value. In 30-nm-thick sacrificial layers, the in-plane lattice parameter remained close to that of the substrate, whereas 120-nm-thick layers relaxed toward the bulk SCAO composition. Consistent with this behavior, the STO thin film grown on a 30-nm-thick SAO showed overlapping film and substrate peaks (Fig. 1g), indicating near lattice matching under these conditions. In contrast, STNNO grown on a 120-nm-thick SAO layer (a_{pc} = 3.961 Å) exhibited a tensile residual strain of +0.5% (Fig. 1i). Similarly, LCNTO on a 120-nm-thick S2C1AO sacrificial layer exhibited compressive strain (−0.5%), and the S2C1AO layer was relaxed, indicating that the LCNTO strain state was primarily determined by mismatch with the relaxed sacrificial layer rather than by substrate clamping transmitted through the sacrificial layer (Fig. 1f).

Note that Ca-rich sacrificial layers can remain strained to the substrate at thicknesses where SAO is relaxed. For the LSCuO film grown on CAO/LAO, the 120-nm-thick CAO layer remained strained to the LAO substrate, yielding an effectively reduced in-plane lattice parameter (~3.78 Å) for the CAO layer and a correspondingly smaller tensile strain of +0.26% in the LSCuO film (Fig. 1h). The contrasting relaxation behavior between 120-nm-thick SAO and 120-nm-thick CAO is consistent with prior reports on this materials family, which have attributed the distinct behavior of Ca-rich compositions to higher elastic stiffness associated with stronger
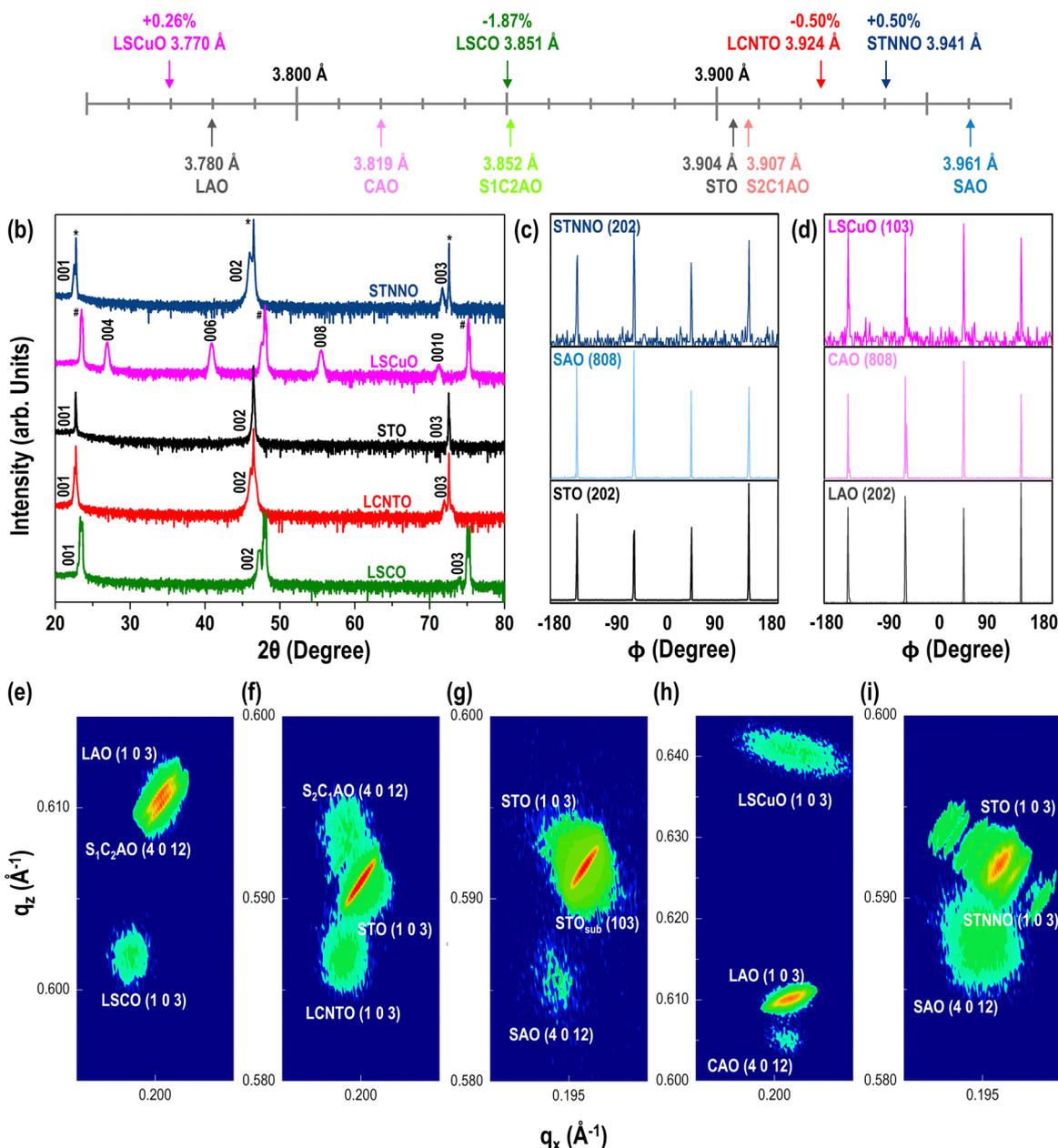
Fig. 1 X-ray diffraction analysis of epitaxial thin films on SCAO-buffered STO and LAO substrates. (a) Lattice parameters of the thin films, SCAO sacrificial layers, and substrates used in this study. (b) Out-of-plane $\theta-2\theta$ scans of 50-nm-thick LSCO, LCNTO, STO, LSCuO, and STNNO films grown on SCAO sacrificial layers with different compositions and thicknesses. The * and # symbols denote the STO and LAO (00l) peaks, respectively. (c) and (d) Representative ϕ scans demonstrating in-plane epitaxial registry among substrate, sacrificial layer, and film. ϕ scans were collected from the substrate {STO: (202)/LAO: (202)}, the sacrificial layer {SAO:(808)/CAO: (808)}, and the film {STNNO: (202)/LSCuO: (103)}. (e)–(i) XRD RSMs around the substrate (103) reflection for STO- and LAO-based heterostructures. Peak positions in q_x and q_z were used to extract lattice parameters and quantify in-plane mismatch/strain and relaxation of the film and sacrificial layer.

Ca–O bonding.[26] In this context, our results indicate that the thickness required for relaxation is strongly composition-dependent in SCAO and should be established experimentally for each stack when strain is used as a design parameter.

These structural results highlight two effective knobs for strain engineering using SCAO sacrificial layers: composition, which sets the nominal lattice parameter, and thickness, which determines whether the sacrificial layer remains clamped to the substrate or relaxes toward its bulk value. This ability to intentionally select strained *versus* relaxed sacrificial layers is central to modulating residual strain in the films and, as discussed in later sections, to understanding how strain relaxation during release influences crack and wrinkle formation in the resulting free-standing membranes.

PPC-supported wet release and transfer of epitaxial oxide membranes

We developed a wet-etch transfer method for transferring single-crystalline oxide thin films onto diverse target substrates using a single spin-coated PPC support layer (Fig. 2). The PPC layer served as a flexible polymer support,[35,43,44,49,50] while membrane release was enabled by wet chemical dissolution of the water-soluble sacrificial layer in DI water[26,43] (Fig. 2a and b). After deposition, PPC was spin-coated on the as-grown heterostructure (Fig. 2c). The sample was then immersed in DI water to dissolve the sacrificial layer and release the oxide film as a PPC-supported membrane (Fig. 2d). The released membrane floated on the water surface (Fig. 2e), enabling transfer onto the target substrate (*e.g.*, Si) while retaining the PPC support during placement (Fig. 2f). The PPC layer was subsequently removed using chloroform at room temperature, yielding the final transferred membrane on the target substrate (Fig. 2g).

This PPC-supported transfer eliminates a heating step for support-layer removal. The support layer was air-dried and removed by solvent, which limited additional thermal exposure during transfer. Spin coating provided continuous, conformal coverage across the film area and supplied mechanical support during release and placement. Because the membrane remained PPC-supported throughout flotation and transfer, it could be positioned in water prior to landing, facilitating handling and placement on diverse substrates. Taken together, the single-layer PPC approach enabled a reduction in process complexity relative to multi-layer supports and provided a practical route for transferring epitaxial oxide membranes onto semiconductor, insulating, and flexible substrates for subsequent structural and transport characterization.

Optimization of the PPC support layer for defect-minimized transfer

Oxide thin films are brittle and mechanically fragile, which complicates their release and handling during wet transfer. A polymer support layer is therefore required to mechanically stabilize the membrane during sacrificial layer dissolution and subsequent placement on the target substrate. We selected PPC as the support material because it provides a compliant, spin-coatable film that can be removed by solvent, and prior studies have reported advantages of PPC over commonly used supports such as polymethyl methacrylate (PMMA) and PDMS.[51–53] Precise control of PPC concentration and spin-coating parameters is crucial for achieving high-quality transfer of brittle oxide membranes as these parameters govern support-layer thickness, continuity, and adhesion during release and removal. In this study, anisole was used as the PPC solvent because it enables uniform spin coating and sufficiently slow drying to form a continuous support film.[54,55] Because PPC thickness and adhesion were expected to vary with spin speed and solution concentration, we optimized the PPC support empirically using the transferred STO membrane quality as the primary metric (Fig. 3), rather than relying on thickness alone.

Fig. 3 summarizes the optimization of the PPC support layer using STO as a model oxide. We evaluated two PPC concentrations (15 and 30 wt%) and a range of spin speeds (1000–5000 rpm, 30 s), then assessed the transferred films on Si by optical microscopy. For 15 wt% PPC (Fig. 3a–e), the transfer quality depended strongly
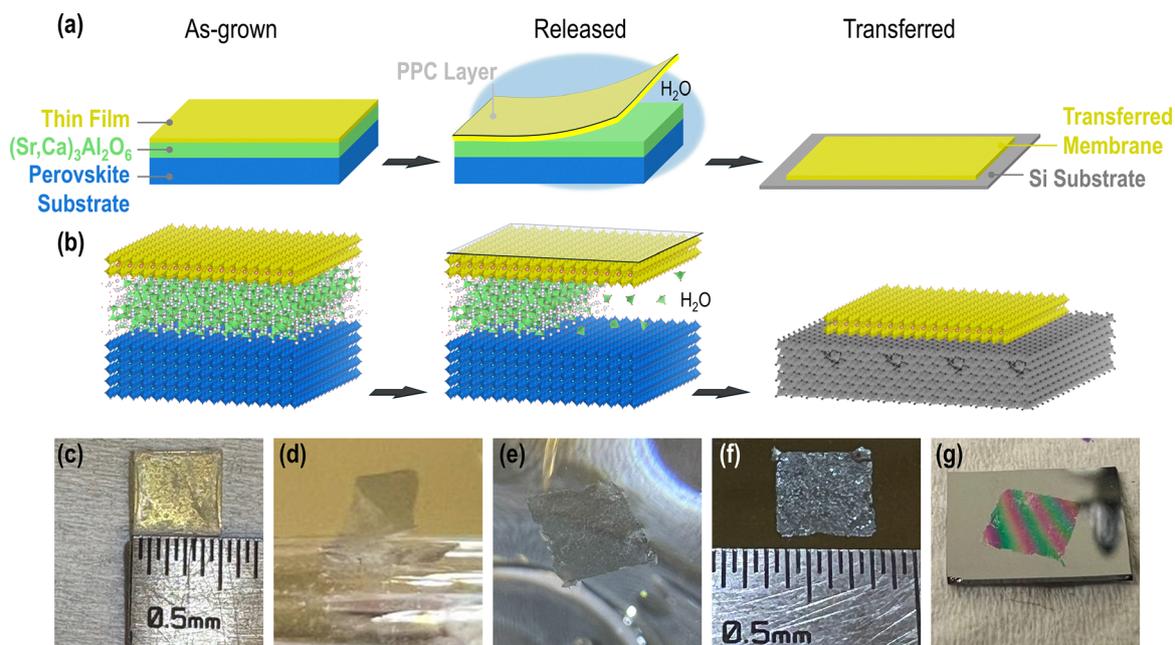

Fig. 2 PPC-supported wet-etch transfer of freestanding epitaxial oxide thin films onto Si using a 30-nm SAO sacrificial layer. (a) Schematic of the transfer sequence developed in this study. (b) Corresponding crystal-structure representations of the film/sacrificial layer/substrate stack at each stage. (c)–(g) Optical images of key steps: (c) as-grown heterostructure after spin-coating PPC, (d) release during dissolution of the SAO sacrificial layer in DI water, (e) PPC-supported membrane floating on the DI water surface, (f) STO membrane transferred onto Si with PPC support retained, and (g) final STO oxide membrane on Si after PPC removal.
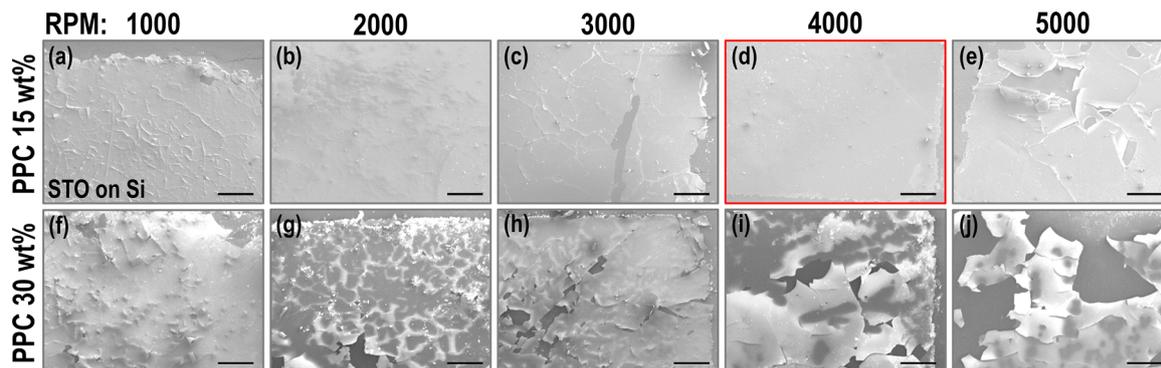
Fig. 3 Optimization of the PPC support layer for transferring STO thin films onto Si using a 30-nm SAO sacrificial layer. (a)–(e) Optical images of transferred STO films using 15 wt% PPC. (f)–(j) Optical images of transferred STO films using 30 wt% PPC. Spin-coating speeds: (a) and (f) 1000, (b) and (g) 2000, (c) and (h) 3000, (d) and (i) 4000, and (e) and (j) 5000 rpm (30 s for all conditions). Scale bars: 300 μm.

on spin speed. At the highest spin speed (5000 rpm), the transferred STO showed clear macroscopic surface damage and discontinuities, consistent with insufficient mechanical support from an overly thin PPC layer (Fig. 3e). At low spin speed (1000 rpm), the transferred surface appeared nonuniform, indicating that an overly thick support layer and/or nonuniform drying can also degrade transfer quality (Fig. 3a). Intermediate spin speeds produced the most uniform transfers. Among these conditions, 4000 rpm yielded the most continuous STO membrane with minimal visible defects in the optical image (Fig. 3d), and was therefore selected as the optimized condition for subsequent transfers.

Increasing PPC concentration to 30 wt% substantially changed the quality of the transferred membranes (Fig. 3f–j). Across the tested spin speeds, the transferred films showed pronounced nonuniformity and extensive damaged or missing regions, particularly at higher speeds (Fig. 3i and j). This behavior is consistent with excessively strong PPC/oxide adhesion and/or difficult support removal, which can promote partial film loss or tearing during the PPC-removal step rather than clean debonding.[48] Based on the comparative trends in Fig. 3, a 15 wt% PPC layer spin-coated at 4000 rpm for 30 s provided the most favorable balance between mechanical support during release and clean removability after transfer (Fig. 3d). This condition was subsequently used as the standard PPC-supported transfer protocol for other oxide systems in this study.

Composition-dependent dissolution and membrane release of SCAO sacrificial layers

The dissolution kinetics of Ca-containing sacrificial layers strongly influenced the release of large-area oxide membranes. Previous studies have reported that Ca-containing layers dissolve more slowly in water than SAO, which has been attributed to stronger Ca–O bonding relative to Sr–O bonding.[26] In the SCAO structure, AlO_2 tetrahedra are surrounded by four Sr–O and Ca–O bonds, which react with water to form $Sr(OH)_2$ and $Ca(OH)_2$, respectively, accompanied by H_2 evolution.[56] On this basis, we systematically compared release behavior across SCAO compositions under identical etching conditions.

Full-stack samples were prepared by depositing 50-nm-thick films of STNNO, LCNTO, LSCO, and LSCuO on 120-nm-thick

SAO, S2C1AO, S1C2AO, and CAO sacrificial layers, respectively. A PPC support layer was spin-coated on each stack, and the samples were immersed in DI water to initiate sacrificial layer dissolution. The release process was monitored by optical microscopy at 6 h, 1 day, 5 days, 10 days, and 15 days for each sacrificial layer composition.

Fig. 4 shows clearly differentiated dissolution and membrane-release behavior as a function of sacrificial layer composition. SAO dissolved rapidly, with substantial dissolution occurring between 1 and 5 days (Fig. 4a–e). S2C1AO dissolved more slowly, with pronounced residual features persisting through 5 days and further advancement by 10 days (Fig. 4f–j). Ca-richer compositions exhibited markedly prolonged behavior, with S1C2AO and CAO showing persistent residual features even at later time points and the slowest progression observed for CAO up to 15 days (Fig. 4k–o and p–t). These observations show that increasing Ca content in SCAO is associated with progressively slower dissolution and delayed release (Fig. 4), consistent with previous studies that have attributed slower dissolution in Ca-containing compositions to stronger Ca–O bonding relative to Sr–O bonding.[26] During dissolution, trapped bubbles were observed beneath the films (Fig. 4b, g, l and q), consistent with H_2 gas evolution during the reaction of the SCAO sacrificial layer with water.[56] As dissolution proceeded, lateral dissolution at the film-sacrificial layer interface advanced across the film footprint until the PPC-supported film detached from the substrate, yielding a freestanding membrane. These results indicate that membrane release time cannot be rationalized by sacrificial layer thickness alone. Even at a fixed sacrificial layer thickness of 120 nm, the dissolution and release behavior varied strongly with SCAO composition. Accordingly, scaling membrane release requires co-optimization of sacrificial layer chemistry and dissolution kinetics, together with the processing time window appropriate for the target membrane area and thickness.

Strain-dependent defect formation in transferred oxide membranes

Fig. 5 shows how the residual strain state of epitaxial oxide thin films on SCAO sacrificial layers relates to membrane integrity after wet release and subsequent transfer. To isolate the role of the membrane itself rather than variability in the support, we
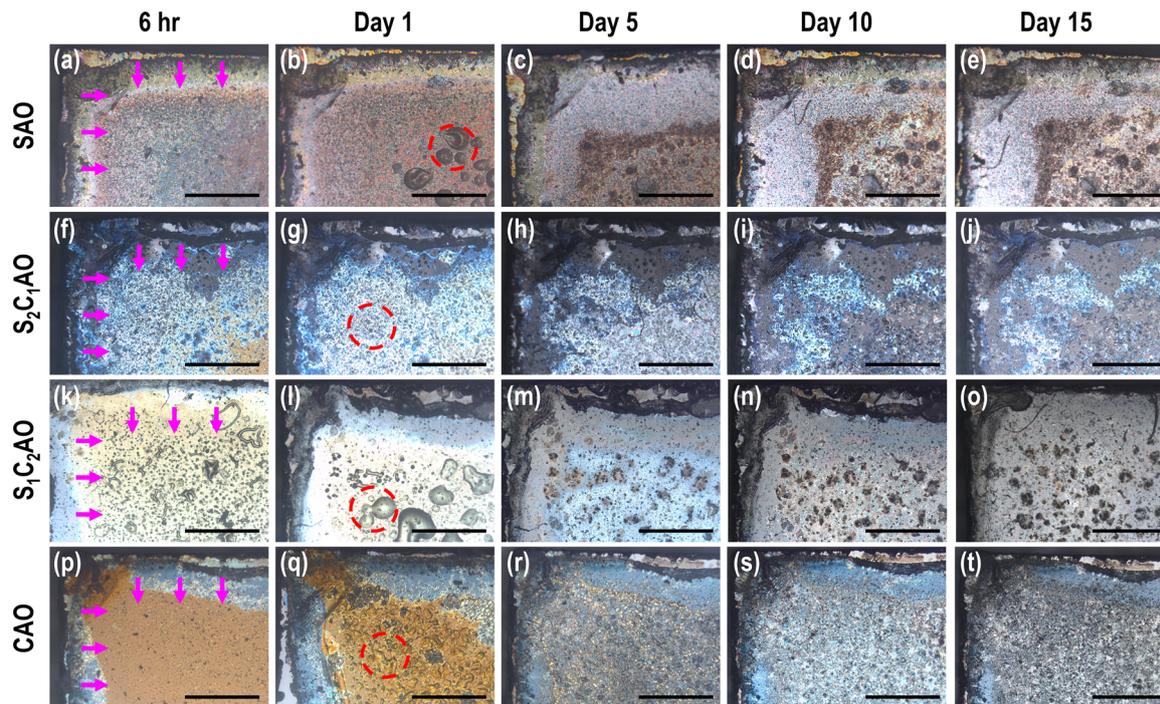
Fig. 4 Time-resolved dissolution of SCAO sacrificial layers during wet release. Optical microscopy images of PPC-coated full stacks immersed in DI water, recorded at 6 h, Day 1, Day 5, Day 10, and Day 15. Rows correspond to sacrificial layer composition: (a)–(e) SAO, (f)–(j) S2C1AO, (k)–(o) S1C2AO, and (p)–(t) CAO (all stacks used 120 nm sacrificial layers). The images capture the color changes that indicate the progression of sacrificial layer dissolution beneath the supported films with regard to the water penetration direction. Trapped bubbles are visible at early stages for several compositions (*e.g.*, b, g, l, q) and are marked with red dashed circles, consistent with gas evolution during the reaction with water. Scale bar: 1 mm.

applied the same PPC support condition to all samples (15 wt% PPC, 4000 rpm, 30 s). Under these fixed support conditions, large-area membranes (~ 25 mm^2) of multiple oxide systems were transferred onto Si without obvious macroscopic tearing or missing regions (Fig. 5a–e). However, higher-magnification optical microscopy and SEM images revealed pronounced, film-dependent microstructural differences after transfer (Fig. 5f–j and k–o).

At the microscale, crack-dominated and wrinkle-dominated morphologies emerged depending on the film/sacrificial layer combination and the associated residual strain. The LSCO membrane released from S1C2AO exhibited a high density of cracks (Fig. 5f and k), consistent with the relatively large lattice mismatch in this stack ($\sim -2\%$). Under strong compressive mismatch, crack networks can segment the membrane into small islands, and local reduction of interfacial contact can cause partial lift-off of some islands, which may appear as flake-like fragments in macroscopic images. In comparison, LCNTO with a smaller compressive residual strain ($\sim -0.5\%$) showed substantially fewer cracks and a more continuous surface (Fig. 5g and l). STO, which was nearly lattice matched when grown on strained SAO, was transferred with minimal visible cracking or wrinkling (Fig. 5h and m). In contrast, the tensile-strained films, STNNO ($\sim +0.5\%$) and LSCuO ($\sim +0.26\%$), developed significant wrinkling upon transfer (Fig. 5i–j and n–o). To rationalize these trends, we note that upon strain release, residual strain is relieved under weak van der Waals contact with the receiver substrate. Tensile-strained membranes tend to relax by in-plane contraction, and

when contraction is constrained by adhesion/friction, the membrane develops an in-plane compressive stress that is relieved by out-of-plane buckling and wrinkling.[57,58] Conversely, compressively strained membranes relax by in-plane expansion, which concentrates tensile stress at defects and promotes crack initiation and propagation into interconnected networks.[27] It is worth noting that LSCuO exhibited more prominent and denser wrinkling than STNNO despite its smaller nominal tensile strain (Fig. 5j and o), suggesting that parameters beyond the nominal mismatch, such as film mechanical response and the strain-relaxation pathway during release, also influence the wrinkle morphology.

A plausible contributor to the wrinkle/crack morphology is the relative stiffness of the oxide membrane, given that the support-layer condition and film thickness were held constant across these comparisons. Prior studies have shown that thin-film deformation patterns in polymer-supported transfers depend on the mechanical compliance of the film/support bilayer, which is governed by elastic modulus and thickness.[59] Using reported values where available, LSCuO has been reported to have a lower Young's modulus (~ 170–180 GPa[60]) than STO (~ 200–250 GPa[31]) and STNNO is expected to be comparable to STO given its titanate-based system. Within this context, the stronger wrinkling observed for LSCuO relative to STNNO (Fig. 5j and o) is consistent with a more compliant membrane undergoing larger out-of-plane deformation during strain relaxation. Similarly, the strong contrast in crack density between LSCO and LCNTO (Fig. 5f, g, k and l) is consistent
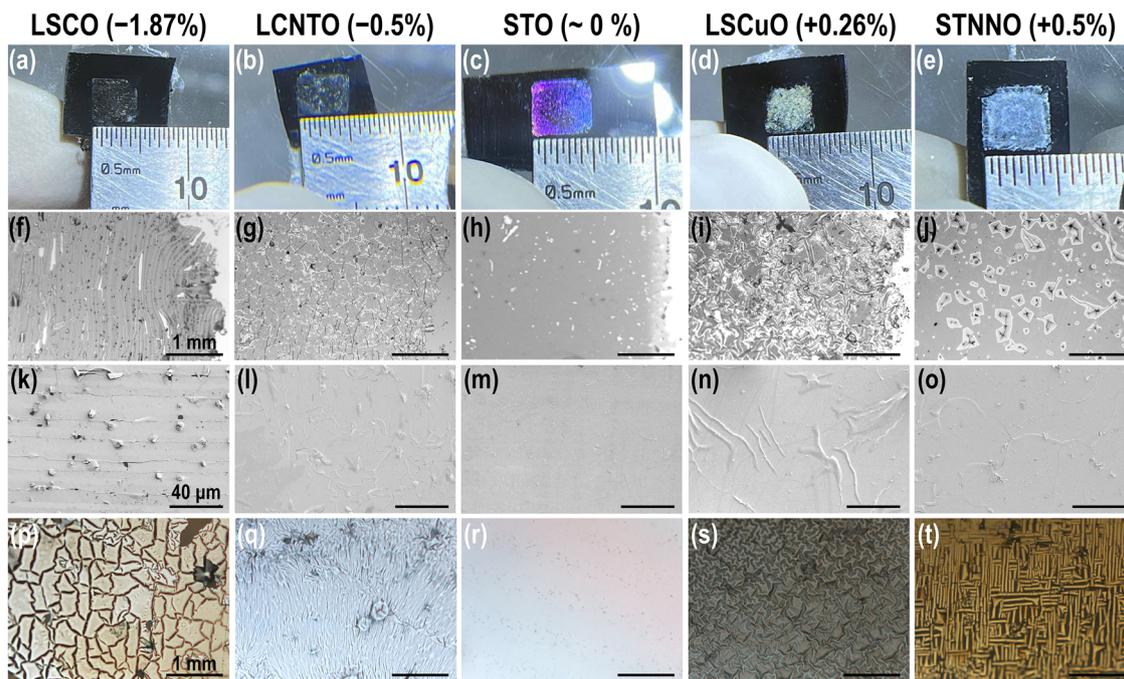
Fig. 5 Strain-dependent defect morphologies in transferred oxide membranes on Si and PI tape using composition- and thickness-engineered SCAO sacrificial layers (see Table S2 for the specific sacrificial layer composition and thickness for each membrane). (a)–(e) Macroscopic photographs of 5×5 mm^2 LSCO, LCNTO, STO, LSCuO, and STNNO membranes after transfer onto Si. The nominal residual strain state for each film is indicated. (f)–(j) Optical microscopy images and (k)–(o) SEM images of the corresponding membranes on Si, highlighting representative crack- and wrinkle-type defects. (p)–(t) Macroscopic photographs of the same membrane set transferred onto PI tape, showing analogous strain-dependent defect formation on a flexible substrate. The non-uniform macroscopic contrast in (a)–(e) is dominated by reflection and thin film interference on the reflective Si substrate. The corresponding optical microscopy and SEM images in (f)–(o) confirm clean membrane surfaces without detectable PPC residue.

with the combined effects of larger mismatch/strain and differences in membrane stiffness, noting that reported elastic moduli for cobaltites can be substantially lower than those of titanate-based oxides.[61,62] Importantly, while these comparisons support a mechanical contribution, disentangling strain magnitude, relaxation pathway, and stiffness would require dedicated mechanical measurements. Accordingly, we interpret Young's modulus as a plausible contributing parameter that helps rationalize the observed differences in wrinkle/crack morphologies, rather than as a sole determinant.

Similar strain-dependent defect morphologies were also observed when membranes were transferred onto polyimide (PI) tape (Fig. 5p–t). Compared with PPC-supported transfer onto Si, direct transfer onto PI imposes different interfacial constraint and compliance, which can alter the way strain relaxation manifests as cracking *versus* wrinkling and can modify wrinkle morphology.[63] Taken together, Fig. 5 establishes that residual strain strongly correlates with the type and density of defects formed during release/transfer, while mechanical compliance of the oxide membrane and the interfacial constraint imposed by the target substrate provide additional control parameters that help rationalize differences among oxide systems.

In addition, structural characterization confirmed that crystallinity and out-of-plane epitaxial orientation were retained after transfer. XRD patterns collected from five representative membranes transferred onto Si (LSCO, LCNTO, STO, LSCuO,

and STNNO) showed well-defined (00*l*) reflections for all samples (Fig. S3a), indicating that epitaxy was maintained after transfer. Representative SEM imaging further demonstrated large-area transfer capability with high uniformity and minimal surface defects. Specifically, a 5×5 mm^2 transferred STO membrane on Si exhibited a uniform surface with minimal visible defects (Fig. S3b). Together, these results support that the PPC-supported wet transfer process enables large-area transfer while maintaining the crystallographic integrity of multiple complex-oxide systems, providing a foundation for the strain-dependent crack/wrinkle trends discussed above.

Transport retention in freestanding membranes and defect-induced degradation

Having established an understanding of how strain relaxation manifests as cracks or wrinkles after transfer, we next examined how these mesoscale defects affected electronic transport. To minimize substrate-related contributions to the measured conductivity, we compared freestanding membranes transferred onto insulating sapphire with relaxed epitaxial reference films grown on insulating LSAT (Fig. S4). Fig. 6 shows the temperature-dependent in-plane conductivity of STNNO, LSCuO, STO, LCNTO, and LSCO for the freestanding membranes and their corresponding epitaxial films. For STO, the membrane on sapphire followed the same conductivity scale and overall temperature dependence as the film on LSAT, indicating that when
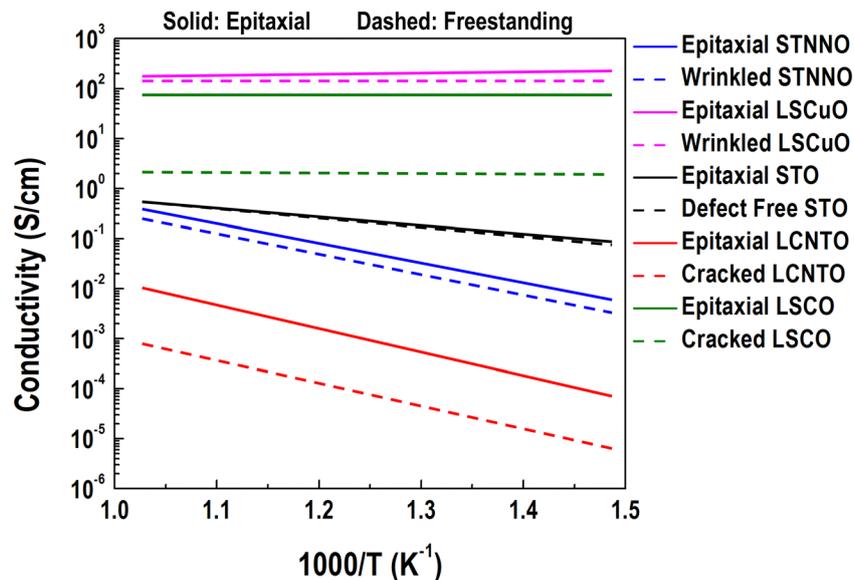
Fig. 6 Temperature–dependent in-plane conductivity of epitaxial films and freestanding membranes. Electrical conductivity of STNNO, LSCuO, STO, LCNTO, and LSCO measured in air from 450 to 700 °C. Solid lines denote relaxed epitaxial films on insulating LSAT, and dashed lines denote the corresponding freestanding membranes transferred onto insulating sapphire to minimize substrate contributions.

macroscopic cracking and wrinkling were minimized (Fig. 5), the release and transfer process preserved film-like in-plane transport. LSCuO also showed closely comparable conductivities for the membrane and film, despite the wrinkling observed after transfer (Fig. 5), suggesting that the wrinkling observed here did not necessarily impose a large penalty on in-plane conduction.

In contrast, pronounced reductions were observed for LCNTO and LSCO after transfer to sapphire. LCNTO membranes exhibited an approximately order-of-magnitude lower conductivity than the LCNTO film across the range, and LSCO membranes showed an even larger drop relative to the highly conducting LSCO film (Fig. 6). These large degradations were consistent with the crack-dominated morphologies seen in the transferred membranes (Fig. 5) because cracks interrupt lateral percolation pathways and segment the membrane into partially isolated conducting regions, introducing high-resistance bottlenecks for in-plane current flow. For the wrinkle-dominated cases (*e.g.*, STNNO and LSCuO), prior work has shown that wrinkles can host nonuniform local strain fields, with tensile strain concentrated near wrinkle apices and relaxing toward the base.[64,65] Such local strain gradients may contribute to the modest, system-dependent deviations in conductivity after transfer observed here, given that tensile strain and defect redistribution can influence carrier mobility in oxide conductors.[66] Collectively, these results indicate that maintaining high conductivity in freestanding oxides requires not only preserved crystallinity, but also suppression of mesoscale mechanical defects, especially cracks, that directly degrade in-plane electrical connectivity.

Conclusion

We demonstrated a scalable route to fabricate and integrate single-crystal complex oxide membranes on silicon, sapphire,

and PI tape, while maintaining epitaxial crystallinity and in-plane transport. The process combines composition- and thickness-engineered water-soluble SCAO sacrificial layers with a single spin-coated PPC support layer, enabling large-area transfer (up to 25 mm^2) without a heating step for support-layer removal. By selecting SCAO chemistry and tuning whether the sacrificial layer remained substrate-clamped or relaxed, we programmed residual strain in diverse perovskite and layered oxides from compressive to tensile and verified the resulting epitaxial crystallinity and residual strain states by HRXRD and RSMs. Time-resolved release studies further established that dissolution and membrane detachment depended strongly on sacrificial layer composition, providing practical guidance for scaling release to larger areas.

Across multiple oxide systems, optical and SEM analyses showed that post-transfer membrane integrity is governed by the coupled effects of residual strain and defect formation, with crack- and wrinkle-dominated morphologies emerging in a strain-dependent manner. Importantly, transport measurements demonstrated that defect-minimized membranes retained film-like in-plane conductivity, whereas cracking and, to a lesser extent, wrinkling degrade conductivity by disrupting lateral connectivity and introducing nonuniform strain fields. Together, these results define a strain-controllable oxide membrane platform that links growth design (sacrificial layer choice and relaxation), release/ transfer mechanics, and resulting electronic performance.

More broadly, this PPC-supported wet transfer strategy expands the accessible materials set beyond prototypical membranes and provides a practical pathway for heterogeneous integration of functional oxides with semiconductor and insulating substrates. The ability to transfer large-area, epitaxial oxide membranes while controlling residual strain and preserving transport establishes a foundation for oxide–silicon integration

and mechanically compliant oxide electronics, and it enables future studies that exploit freestanding geometries for strain engineering and device architectures not achievable in substrate-clamped films.

Author contributions

Habib Rostaghi Chalaki: investigation (lead); writing – original draft (lead). Ebenezer Seesi: investigation (supporting); writing – review & editing (supporting). Avari Suber: investigation (supporting); writing – review (supporting). Sang-Hoon Nam: investigation (supporting); writing – review & editing (supporting). Yo-Han Suh: data curation; writing – review & editing (supporting). Dongkyu Lee: conceptualization (lead); funding acquisition (lead); supervision (lead); writing – review & editing (lead).

Conflicts of interest

There are no conflicts to declare.

Data availability

All data supporting the findings of this study are available within the article and its supplementary information (SI). Supplementary information is available. See DOI: https://doi.org/10.1039/d5ma01530h.

Acknowledgements

References

1 Y. Hao, T. Li and X. Hong, *Chem. Commun.*, 2025, **61**, 4924–4950.

2 W. Li, J. Shi, K. H. Zhang and J. L. MacManus-Driscoll, *Mater. Horiz.*, 2020, **7**, 2832–2859.

3 H. Kum, D. Lee, W. Kong, H. Kim, Y. Park, Y. Kim, Y. Baek, S.-H. Bae, K. Lee and J. Kim, *Nat. Electron.*, 2019, **2**, 439–450.

4 R. Scherwitzl, S. Gariglio, M. Gabay, P. Zubko, M. Gibert and J. M. Triscone, *Phys. Rev. Lett.*, 2011, **106**, 246403.

5 H. Lu, L. Li, Z. Tang, M. Xu, Y. Zheng, M. Becker, Y. Lu, M. Li, P. Li, Z. Zhang, P. J. Klar and Y. He, *Appl. Phys. Lett.*, 2023, **123**, 042103.

6 S. Catalano, M. Gibert, J. Fowlie, J. Íñiguez, J. Triscone and J. Kreisel, *Rep. Prog. Phys.*, 2018, **81**, 046501.

7 G. Yang, S.-H. Nam, G. Han, N. X. Fang and D. Lee, *ACS Appl. Mater. Interfaces*, 2023, **15**, 50427–50436.

8 G. Yang, M. El Loubani, H. R. Chalaki, J. Kim, J. K. Keum, C. M. Rouleau and D. Lee, *ACS Appl. Electron. Mater.*, 2023, **5**, 4556–4563.

9 G. Yang, M. El Loubani, D. Handrick, C. Stevenson and D. Lee, *Solid State Ionics*, 2023, **393**, 116171.

10 G. Yang, M. El Loubani, D. Hill, J. K. Keum and D. Lee, *Catal. Today*, 2023, **409**, 87–93.

11 T. L. Meyer, R. Jacobs, D. Lee, L. Jiang, J. W. Freeland, C. Sohn, T. Egami, D. Morgan and H. N. Lee, *Nat. Commun.*, 2018, **9**, 92.

12 C. Eom, A. Marshall, S. Laderman, R. Jacowitz and T. Geballe, *Science*, 1990, **249**, 1549–1552.

13 N. Reyren, S. Thiel, A. Caviglia, L. F. Kourkoutis, G. Hammerl, C. Richter, C. W. Schneider, T. Kopp, A.-S. Ruetschi and D. Jaccard, *Science*, 2007, **317**, 1196–1199.

14 R. Zeches, M. Rossell, J. Zhang, A. Hatt, Q. He, C.-H. Yang, A. Kumar, C. Wang, A. Melville and C. Adamo, *Science*, 2009, **326**, 977–980.

15 R. Ramesh and N. A. Spaldin, *Nat. Mater.*, 2007, **6**, 21–29.

16 J. Wang, J. Neaton, H. Zheng, V. Nagarajan, S. Ogale, B. Liu, D. Viehland, V. Vaithyanathan, D. Schlom and U. Waghmare, *Science*, 2003, **299**, 1719–1722.

17 D. G. Schlom, L. Q. Chen, X. Pan, A. Schmehl and M. A. Zurbuchen, *J. Am. Ceram. Soc.*, 2008, **91**, 2429–2454.

18 J. M. Phillips, *MRS Bull.*, 1995, **20**, 35–39.

19 D. G. Schlom, L.-Q. Chen, C. J. Fennie, V. Gopalan, D. A. Muller, X. Pan, R. Ramesh and R. Uecker, *MRS Bull.*, 2014, **39**, 118–130.

20 D. Ji, S. Cai, T. R. Paudel, H. Sun, C. Zhang, L. Han, Y. Wei, Y. Zang, M. Gu and Y. Zhang, *Nature*, 2019, **570**, 87–90.

21 Y. Li, C. Xiang, F. M. Chiabrera, S. Yun, H. Zhang, D. J. Kelly, R. T. Dahm, C. K. Kirchert, T. E. L. Cozannet and F. Trier, *Adv. Mater.*, 2022, **34**, 2203187.

22 E. Brand, P. Salles, A. Palliotto, H. Wang, W. Chen, E. Dollekamp, M. Ramis, Q. Li, J. Drnec and J. M. García-Lastra, *Adv. Phys. Res.*, 2025, **4**, e00075.

23 D.-S. Park and N. Pryds, *J. Mater. Res.*, 2024, **39**, 2907–2917.

24 S. Choo, S. Varshney, H. Liu, S. Sharma, R. D. James and B. Jalan, *Sci. Adv.*, 2024, **10**, eadq8561.

25 D. Lu, D. J. Baek, S. S. Hong, L. F. Kourkoutis, Y. Hikita and H. Y. Hwang, *Nat. Mater.*, 2016, **15**, 1255–1260.

26 S. Yun, T. E. le Cozannet, C. H. Christoffersen, E. Brand, T. S. Jespersen and N. Pryds, *Small*, 2024, 2310782.

27 L. Gong, M. Wei, R. Yu, H. Ohta and T. Katayama, *ACS Nano*, 2022, **16**, 21013–21019.

28 M. Li, Z. Wang, G. Xiong, S. Fan, Q. Zhao and K. Lin, *Thin Solid Films*, 2000, **375**, 271–274.

29 D. H. Blank, G. Koster, G. A. Rijnders, E. Van Setten, P. Slycke and H. Rogalla, *J. Cryst. Growth*, 2000, **211**, 98–105.

30 H. Mei, Y. Pang, S. H. Im and R. Huang, Fracture, delamination, and buckling of elastic thin films on compliant substrates, *2008 11th Intersociety Conference on Thermal and Thermomechanical Phenomena in Electronic Systems*, Orlando, FL, 2008, pp. 762–769, DOI: 10.1109/ITHERM.2008.4544345.

31 Q. Meng, J. Shi, J. Zhang, Y. Liu, W. Wang, R. F. Webster, D. Zhao, Y. Zhu, B. Hao and B. Qu, *ACS Appl. Mater. Interfaces*, 2024, 28980–28990.

32 Y. Han, J. Guo, H. Liu, J. Wang, W. Gao, Q. Wang, B. He and W. Lue, *Ceram. Int.*, 2024, **50**, 52474–52479.

33 R. Xu, J. Huang, E. S. Barnard, S. S. Hong, P. Singh, E. K. Wong, T. Jansen, V. Harbola, J. Xiao and B. Y. Wang, *Nat. Commun.*, 2020, **11**, 3141.

34 V. Harbola, R. Xu, S. Crossley, P. Singh and H. Y. Hwang, *Appl. Phys. Lett.*, 2021, **119**, 053102.

35 Y. Zhao, R. Peng, Y. Guo, Z. Liu, Y. Dong, S. Zhao, Y. Li, G. Dong, Y. Hu and J. Zhang, *Adv. Funct. Mater.*, 2021, **31**, 2009376.

36 H. Elangovan, M. Barzilay, S. Seremi, N. Cohen, Y. Jiang, L. W. Martin and Y. Ivry, *ACS Nano*, 2020, **14**, 5053–5060.

37 E. Brand, C. Hoegfeldt, A. Palliotto, I. V. Maznichenko, D. Rata, S. Ostanin, J. Chen, S. Lounis, K. Doerr, A. Ernst, S. Kadkhodazadeh, N. Pryds and D.-S. Park, *ACS Nano*, 2025, **19**, 41172–41183.

38 J. Zhang, T. Lin, A. Wang, X. Wang, Q. He, H. Ye, J. Lu, Q. Wang, Z. Liang, F. Jin, S. Chen, M. Fan, E.-J. Guo, Q. Zhang, L. Gu, Z. Luo, L. Si, W. Wu and L. Wang, *Science*, 2024, **383**, 388–394.

39 G. Dong, S. Li, T. Li, H. Wu, T. Nan, X. Wang, H. Liu, Y. Cheng, Y. Zhou and W. Qu, *Adv. Mater.*, 2020, **32**, 2004477.

40 S. Varshney, M. Ramis, S. Choo, M. Coll and B. Jalan, *J. Mater. Chem. C*, 2024, **12**, 13809–13815.

41 S. Varshney, S. Choo, L. Thompson, Z. Yang, J. Shah, J. Wen, S. J. Koester, K. A. Mkhoyan, A. McLeod and B. Jalan, *ACS Nano*, 2024, **18**, 6348–6358.

42 P. Singh, A. Swartz, D. Lu, S. S. Hong, K. Lee, A. F. Marshall, K. Nishio, Y. Hikita and H. Y. Hwang, *ACS Appl. Electron. Mater.*, 2019, **1**, 1269–1274.

43 B. Zhang, C. Yun and J. L. MacManus-Driscoll, *Nano-Micro Lett.*, 2021, **13**, 1–14.

44 K. Gu, T. Katayama, S. Yasui, A. Chikamatsu, S. Yasuhara, M. Itoh and T. Hasegawa, *Adv. Funct. Mater.*, 2020, **30**, 2001236.

45 C. Yu, M. Zhang, L. Liang, L. Qin, Y. Chen, Y. Lei, Y. Wang, Y. Song, C. Qiu, P. Jia, D. Li and L. Wang, *Light: Sci. Appl.*, 2025, **14**, 396.

46 R. Guo, L. You, W. Lin, A. Abdelsamie, X. Shu, G. Zhou, S. Chen, L. Liu, X. Yan, J. Wang and J. Chen, *Nat. Commun.*, 2020, **11**, 2571.

47 D. Lu, S. Crossley, R. Xu, Y. Hikita and H. Y. Hwang, *Nano Lett.*, 2019, **19**, 3999–4003.

48 F. M. Chiabrera, S. Yun, Y. Li, R. T. Dahm, H. Zhang, C. K. Kirchert, D. V. Christensen, F. Trier, T. S. Jespersen and N. Pryds, *Ann. Phys.*, 2022, **534**, 2200084.

49 G. Dong, S. Li, M. Yao, Z. Zhou, Y.-Q. Zhang, X. Han, Z. Luo, J. Yao, B. Peng and Z. Hu, *Science*, 2019, **366**, 475–479.

50 R. Li, Y. Xu, J. Song, P. Wang, C. Li and D. Wu, *Appl. Phys. Lett.*, 2020, 116.

51 L. Wang, Y. Li, J. Yang, Q. Wu, S. Liang and Z. Liu, *Int. J. Mol. Sci.*, 2024, **25**, 2938.

52 D. Dong, S. S. Dhanabalan, P. F. M. Elango, M. Yang, S. Walia, S. Sriram and M. Bhaskaran, *Appl. Phys. Rev.*, 2023, **10**, 031314.

53 Y. Mouhamad, P. Mokarian-Tabari, N. Clarke, R. Jones and M. Geoghegan, *J. Appl. Phys.*, 2014, 116.

54 J. S. Jaworski, M. Cembor and M. Orlik, *J. Electroanal. Chem.*, 2005, **582**, 165–170.

55 C. N. Carvalho, M. D. S. Lanza, L. G. Dourado, E. M. Carvalho and J. Bauer, *Int. J. Dent.*, 2019, **2019**, 5496784.

56 Q. Lu, Z. Liu, Q. Yang, H. Cao, P. Balakrishnan, Q. Wang, L. Cheng, Y. Lu, J.-M. Zuo and H. Zhou, *ACS Nano*, 2022, **16**, 7580–7588.

57 T. Jiang, R. Huang and Y. Zhu, *Adv. Funct. Mater.*, 2014, **24**, 396–402.

58 D. J. Lipomi, M. Vosgueritchian, B. C. K. Tee, S. L. Hellstrom, J. A. Lee, C. H. Fox and Z. Bao, *Nat. Nanotechnol.*, 2011, **6**, 788–792.

59 Y. Lei, Y. Chen, R. Zhang, Y. Li, Q. Yan, S. Lee, Y. Yu, H. Tsai, W. Choi and K. Wang, *Nature*, 2020, **583**, 790–795.

60 D. Pelc, Z. Anderson, B. Yu, C. Leighton and M. Greven, *Nat. Commun.*, 2019, **10**, 2729.

61 A. Aman, Y. Chen, M. Lugovy, N. Orlovskaya, M. J. Reece, D. Ma, A. D. Stoica and K. An, *J. Appl. Phys.*, 2014, **116**, 013503.

62 M. Rabiei, A. Palevicius, S. Nasiri, A. Dashti, A. Vilkauskas and G. Janusas, *Materials*, 2021, **14**, 1258.

63 Y. Su, A. Zong, A. Kogar, D. Lu, S. S. Hong, B. Freelon, T. Rohwer, B. Y. Wang, H. Y. Hwang and N. Gedik, *Nano Lett.*, 2023, **23**, 10772–10778.

64 Y. Koo, Y. Kim, S. H. Choi, H. Lee, J. Choi, D. Y. Lee, M. Kang, H. S. Lee, K. K. Kim and G. Lee, *Adv. Mater.*, 2021, **33**, 2008234.

65 V. Rahneshin, D. A. Ziolkowska, A. McClelland, J. Cromwell, J. B. Jasinski and B. Panchapakesan, *Sci. Rep.*, 2018, **8**, 64.

66 M. Tyunina, M. Savinov, O. Pacherova, T. Kocourek, P. Yudin and A. Dejneka, *APL Mater.*, 2025, **13**, 031101.